Enhancement of toughness of Al-to-steel Friction Melt Bonded welds via metallic interlayers

Enhancement of toughness of Al-to-steel Friction Melt Bonded welds via metallic interlayers

Norberto Jimenez-Mena[1], Pascal J. Jacques[1], Lipeng Ding[1,2], Nicolas Gauquelin[2], Dominique Schryvers[2], Hosni Idrissi[1,2], Francis Delannay[1], Aude Simar[1]

[1]Université catholique de Louvain, Institute of Mechanics, Materials and Civil Engineering, IMAP, 1348 Louvain-la-Neuve, Belgium
[2]Electron Microscopy for Materials Science (EMAT), Department of Physics, University of Antwerp, Groenenborgerlaan 171, B-2020 Antwerp, Belgium

Abstract

The toughness of Al-to-steel welds decreases with increasing thickness of the intermetallic (IM) layer formed at the interface. Co plating has been added as interlayer in Al-to-steel Friction Melt Bonded (FMB) welds to control the nature and thickness of the IM layer. In comparison to a weld without interlayer, Co plating brings about a reduction of the thickness of the IM layer by 70%. The critical energy release rate of the crack propagating in the weld is used as an indicator of toughness. It is evaluated via an adapted crack propagation test using an energy conservation criterion. For a weld without interlayer, critical energy release rate is found to increase when the thickness of the intermetallic layer decreases. When the intermetallic layer is thick, the crack propagates in a brittle manner through the intermetallic whereas, at low layer thickness, the crack deviates and partially propagates through the Al plate, which causes an increase of toughness. The use of a Co interlayer brings about an increase of toughness by causing full deviation of the crack towards the Al plate.

Keywords: Dissimilar welding; Friction Melt Bonding; Aluminium; Steel; interlayer; Toughness

1. Introduction

Multi-material designing is seen as a key strategy to reduce the weight of automobiles, and by extension greenhouse gas emissions, while keeping high levels of crashworthiness [1]. The joining of Al to steel looks particularly interesting owing to the combination of the high strength of steel and the low density of aluminium. Nevertheless, the welding of Al to steel is challenging due to the large differences in physical properties (melting temperature, thermal expansion coefficient …) and to the formation of a brittle intermetallic (IM) layer at the interface between Al and steel [2]. Two iron aluminides compose this IM layer: Fe_2Al_5 is usually formed on the steel side while Fe_3Al_{14} (also referred to as $FeAl_3$ [3]) is usually formed on the aluminium side [4,5,6].

The IM layer is the prominent microstructural feature affecting the mechanical properties of an Al-to-steel welds. Tanaka *et al.* [4] observed that reducing the thickness of the IM layer leads to an increase of the strength of friction stir welds. They stated that IM thicknesses below 1 µm result in tough welds. The growth kinetics of the IM layer at the Al-steel interface follows a parabolic law with constants depending on the composition of the base materials and on temperature [6,7,8]. A strategy to reduce the thickness of the IM layer is to reduce time and temperature spent at high temperatures. Solid-state welding techniques such as Friction Welding (FW), Friction Stir Welding (FSW) and diffusion bonding bring low IM growth rates owing to a process temperature below the melting point of the aluminium alloy. IM layer thicknesses of the order of 1 µm can thus easily be achieved [4,9]. On the other hand, liquid-state welding techniques such as arc welding, laser welding and resistance welding involve large IM layer growing rates [10,11,12,13], but might allow larger welding speeds due to the larger reactivity compared to solid state welding. Hence, controlling IM layer thickness through the control of the temperature/time profile is rather challenging for liquid-state processing routes.

The reactivity between Al and steel can be controlled by adding alloying elements in the base materials or by placing interlayers between them. Yin *et al.* [7] modified the growth rate of the Al/Fe intermetallic phases in the case of hot dipping of steel into liquid aluminium by increasing the concentration of Si in liquid aluminium. Ikeuchi *et al.* [14] and Hwang *et al.* [15] observed that, during hot dipping of steel into liquid aluminium, the growth rate of the IM layer decreased with increasing concentration of carbon in the steel plate. In friction welding, Reddy *et al.* [16] suppressed the formation of Fe/Al compounds using Cu, Ni and Ag coatings as interlayers. Cu, Ni and Ag aluminides formed at the interface, which increased the strength of the weld under tensile and flexion loading. The use of interlayers is not limited to Al-to-steel welding. Sahu *et al.* [17] observed that the addition of a Ti interlayer in FSW of Al-to-Cu suppressed the formation of Al/Cu IM phases and increased the strength of the weld under tensile loading.

In the present work, Friction Melt Bonding (FMB) is used to weld aluminium to steel in lap-joint configuration [5,6,18,19]. FMB is a liquid state technique that takes advantage of the large differences in melting temperature of the materials to be bonded. In this process, schematized in Fig. 1(a), the steel plate is placed on top of an aluminium plate and the plates are clamped together. A rotating flat cylindrical tool is pressed against the steel surface, generating heat by friction and deformation on the top surface of the steel. The generated heat leads to an increase of temperature in the steel plate up to between the melting temperatures of steel and aluminium. Hence, the aluminium alloy in contact with the steel plate locally melts and reacts with the solid steel to form an IM layer. The tool moves on the surface of the steel plate to form a continuous welding seam. No protective gas flux is required since the Al-based molten pool and the reaction with the steel are confined without contact with the atmosphere.

To study the effect of Co interlayers on the growth kinetics and mechanical properties of IM layers, Co interlayers were electroplated on steel plates prior to welding. The evolution of the thickness of the IM layer was fitted by a parabolic growth law. The critical energy release rate was assessed by means of an adapted crack propagation test using an energy conservation criterion. Differences in critical energy release rate are used as toughness difference indicator. Discussion highlights the dependence of fracture mechanisms on IM layer thickness.

2. Thermal Finite Element Modelling and IM layer growth

The temperature/time profile at the Al-steel interface is needed to estimate the kinetics of the IM layer growth. A heat-transfer finite element model has thus been adapted from the work of Crucifix *et al.* [6] and implemented in Abaqus [20]. The steel and aluminium plates, the backing plate and the welding table are modelled as shown on Fig. 2(a). The power input at the tool contact is inferred from the torque measurements carried out during welding using [6]

$$P = \eta(T_z \cdot \omega) \quad (1)$$

where T_z is the torque, ω is the rotational speed and $\eta \in [0,1]$ is the efficiency parameter (Table 1) [6]. The inferred power input is provided in Table 3. The value of efficiency parameter, η = 0.9, is taken from the work of Crucifix *et al.* [6] accounting for the similarities of the welding conditions. Low conducting and high conducting contact interfaces are distinguished at the interface between the plates. The high conducting contact interfaces are the steel-aluminium interface below the tool, the steel-aluminium interface where the IM bonding is formed, and the aluminium-backing plate interface below the tool. These interfaces are given an infinitely large conductance value (arbitrarily set to 10^6 kW.m^{-2}.K^{-1} in Abaqus), which yields no difference of temperature between the sides of these interfaces. For the rest of the contact surfaces, the conductance is set to the low value calibrated by Crucifix *et al.* [6], i.e. 10 kW.m^{-2}.K^{-1}. The emissivity of the system is set to 0.3 and the convection coefficient is

set to 15 $W.m^{-2}.K^{-1}$ [21,22]. The curves in Figs. 2(b, c, d) show the temperature profiles calculated above the solidus temperature of AA1050 at three distances from the weld centreline (0 mm, 2 mm and 4 mm) for the three experimentally tested welding speeds (300, 500 and 700 $mm.min^{-1}$), respectively. The maximum temperatures reached and the reaction times increase as the welding speed decreases. This model has been further validated in a previous publication [19].

According to Tanaka *et al.* [8], the growth of the IM layer in the reaction between iron and molten aluminium follows a parabolic law:

$$X(\theta, t) = \sqrt{k(\theta) \cdot t} \quad (2)$$

where X is the thickness of the IM layer, $k(\theta)$ is a constant and t is time. Tanaka *et al.* [8] used an Arrhenius law to account for the effect of temperature on the growing kinetics of the IM layer:

$$k(\theta) = k_o \cdot e^{\left(\frac{-Q}{R \cdot \theta}\right)} \quad (3)$$

where k_o is the pre-exponential factor, Q is the activation energy, R is the gas constant and θ is the temperature. k_o and Q are fitted with a least squares procedure exploiting the temperature profile estimated at the interface and provided in Figs. 2(b, c, d).

3. Crack propagation test and analysis

The crack propagation resistance was evaluated by means of a cantilever bending test. A schematic drawing of the test is shown in Fig. 1(b). Two specimens per weld of 8x50 mm were extracted by electric-discharge machining (EDM) from the part of the weld where the two plates are completely bonded. A notch was machined at the Al-steel interface by EDM. The specimen was fastened to the holder using 5 holes passing in the aluminium plate in which rods of 1.5 mm diameter were inserted. A vertical hole was drilled in the aluminium plate below the notch for allowing passage of a rod that pushes the steel plate away from the

fastened aluminium plate in order to propagate a crack at the interface. The displacement and load were measured on the rod. The test was recorded by a video camera with a frame period of 4 seconds and a resolution of 70 pixels.mm^{-1}.

The critical energy release rate, Γ, dissipated during the propagation of the crack was estimated using an energy conservation principle. The energy introduced in the system corresponds to the work exerted by the testing machine, calculated as the integral of the load-displacement curve of the pushing rod. 4 different contributions have been identified to dissipated the energy exerted by the testing machine as the crack propagates: (i) the energy dissipated in the deformation of the steel beam, W_{steel}, (ii) the energy dissipated in the deformation of the Al plate, W_{Al}, (iii) the energy dissipated by friction at the contact between the pushing rod and the steel beam, $W_{friction}$, and (iv) the energy dissipated in the propagation of the crack, $b \cdot \Gamma \cdot a$, where b is the width of the specimen, Γ is the critical energy release rate of the assembly and a is the crack length. The equation for energy conservation as the crack advances is thus

$$\frac{dE}{da} = \frac{dW_{steel}}{da} + \frac{dW_{Al}}{da} + \frac{dW_{friction}}{da} + b \cdot \Gamma \quad (4)$$

where, E is the work exerted by the testing machine and da is the crack advancement.

The energy dissipated in plastic bending of the steel beam can be assessed from the radius of curvature using the elasto-plastic beam theory, as suggested by Rimovskis *et al.* [23]. The radius of curvature along the steel plate was measured on the images provided by the video camera using a least squares fitting procedure. Only bending is considered: shearing and longitudinal forces on the beam are neglected. The deformation energy in the steel beam is obtained by integration of the product of strain and stress in the analysed volume [24]

$$W_{steel} = b \cdot \int_0^a \int_{-\frac{h}{2}}^{\frac{h}{2}} (\varepsilon \cdot \sigma + \gamma \cdot \tau) \cdot dz \cdot dx \quad (5)$$

where h is the thickness of the beam, ε and γ are the longitudinal strain in the x direction and the shear strain, respectively, and σ and τ are the longitudinal stress in the x direction and the shear stress, respectively. Owing to the small thickness of the steel beam (0.9 mm thick), a slenderness approximation is used and shear is neglected. In pure beam bending, the strain increases linearly with the distance from the neutral axis, which is supposed to remain at mid-thickness of the beam. Therefore, the strain, ε, is calculated as [23]

$$\varepsilon = \frac{z}{\rho} \quad (6)$$

where z is the distance from the neutral axis and ρ is the radius of curvature. The mechanical properties of the steel after welding were measured from tensile testing of specimens machined from steel plates that had been previously welded to and detached from an aluminium plate. The tensile test was carried out at a constant cross head speed of 2 mm.s^{-1}. σ is obtained from the stress-strain curve of the steel plate at a given tensile strain ε.

The energy dissipated by friction between the pushing rod and the steel beam, $W_{friction}$, is estimated from a Coulomb's friction law [25]:

$$W_{friction} = \mu \cdot F_{\perp} \cdot l \quad (7)$$

where μ is the friction coefficient, $F_{\perp}$ is the load applied by the rod perpendicular to the steel beam, and l is the relative displacement of rod and steel beam measured on video images. As represented in Fig. 1(b), the contact angle, φ, between the surface of the steel beam and the pushing rod (represented by an arrow F_{rod}) is not constant. At the beginning of the test, the rod is perpendicular to the steel beam, $\varphi = 90°$, but it decreases monotonously. Therefore, $F_{\perp} = F_{rod} \cdot \cos(\varphi)$, where the contact angle, φ, is measured on video images. The friction coefficient, μ, at the contact between the rod and the steel plate was measured by means of a Bruker tribometer at three different travel speeds (0.1, 0.05 and 0.025 mm.s^{-1}) and 6 different vertical loads (20, 50, 100, 200, 300 and 400 N) to cover the contact conditions during the

crack propagation test. Prior to the tests, the steel surface was machined by EDM in such a way as to present the same surface characteristics as in the crack propagation specimen.

The evolution of the energy dissipated in the Al during the propagation, $\frac{dW_{Al}}{da}$, is unknown since the aluminium plate is partially hidden by the holding device. From the video images, it could be observed that the macro-deformation of the aluminium plate mostly occurs before the crack starts to propagate and that the plate remains fairly static during the crack propagation stage. It is thus assumed that W_{Al}, and thus also $\frac{dW_{Al}}{da}$, are negligible during crack propagation.

Tests were completed by longitudinal observations of cross sections of the assembly in order to reveal the crack path. Fracture surfaces were analysed by scanning electron microscopy to determine the type and location of the crack path.

4. Materials processing and characterisation

Base materials were AA1050 aluminium alloy and Dual-Phase steel (DP600) with respective thicknesses of 3.0 and 0.9 mm. Their compositions are given in Table 2. The plates were cut to a size of 200x80 mm. Friction melt bonding was carried out on a Hermle milling machine. The tool was a cylinder of cemented tungsten carbide (WC-Co) with 16 mm diameter. The tool had a backwards tilting angle of 0.5º and its rotational speed was 2000 rpm. The welding speeds were 300, 500 and 700 mm.min^{-1}, respectively. To keep a good contact between the tool and the steel plate, the plunge of the tool was increased along with the welding speed (Table 3). The torque on the tool was measured with a Kistler dynamometer.

Co was electroplated on the steel plate using the solution and conditions listed in Tables 4 and 5 [26]. The areas to be coated were delimited with scotch tape. The thickness of the plating was 5 µm. Two different assemblies are designated according to the main element in

contact with the liquid aluminium: Fe-Al assembly for the weld without interlayer and Co-Al assembly for welds performed with cobalt interlayer.

The thickness of the IM layer at different positions from the weld centreline was measured by SEM observations in transversal cuts. Transmission electron microscopy (TEM) was used to identify the phases formed at the interfaces. TEM specimens were cut from the joining interface of the three systems using a dual-beam focused ion beam (FIB) instrument (FEI Helios Nanolab 650). Scanning TEM energy dispersive X-ray (STEM-EDX) elemental maps as well as selected area electron diffraction (SAED) patterns were acquired in a FEI Osiris TEM operated at 200kV and equipped with a CHEMISTEM detector. A dedicated analytical holder was used for the EDX measurements.

5. Results

5.1. IM phase identification

Fig. 3 illustrates the dependence on welding speed of the IM layer thickness at the weld centreline for the Fe-Al, and Co-Al systems, respectively. The thickness of the layer clearly decreases with increasing welding speed. Both systems show homogeneous IM layer. Hot tears were observed in the re-solidified aluminium molten pool at a speed of 700 $mm.min^{-1}$ for the Co-Al system. Hot tears are cracks developing at the grain boundary due to the contraction strains of the aluminium alloy during the solidification. Their formation is linked to the composition of the aluminium and to the thermomechanical cycles carried out during processing [19,27].

Fig. 4 shows the identification of the IM phases using STEM-EDX elemental maps and SAED patterns. In both systems, the IM layer is composed of two phases, as shown in Fig. 4 and listed in Table 6. For the Fe-Al system, Fe_4Al_{13} grows on the Al side while Fe_2Al_5 grows on the steel side. For the Co-Al system, Co_2Al_9 is observed on the Al side while $CoAl_3$ is found on the Co plating side. From Fig. 4 and Table 6, it can be concluded that EDX

measurements are in good agreement with the crystallographic identification of the phases by SAED. The presence of Fe in IM3 and IM4 in Table 5 is explained by the presence of 0.38%wt. Fe in the liquid aluminium. Due to the very low solubility of Fe in Al [8], the Fe is rejected from the growing Al grains during solidification and incorporated in the IM phase. In addition, 1.2 %wt. Fe is measured in the Co plating after welding. This Fe can also be incorporated in the IM layer.

5.2. IM growth

IM thickness was measured every 0.33 mm in a width of ±4 mm from the weld centreline. As mentioned in the previous sub-section, two IM phases are formed. The thickness measurement thus includes both phases. Thickness variation as a function of the distance from the weld centreline is shown in Fig. 5 for the different welds. IM layer thickness decreases when welding speed increases and is always maximum at the weld centreline. For a given welding speed, layer thickness is lower in the Co-Al system than in the Al-Fe system.

The constants k_o and Q of Eq. 3 can be derived by fitting the thickness values provided shown in Fig. 5 using the temperature profiles calculated via the FE simulations (Fig. 2). The constants ensuing from this fitting procedure are given in Table 7 and the corresponding simulated curves are shown as continuous lines in Fig. 5.

5.3. Crack propagation testing

Fig. 6 shows frames of the videos recorded during the crack propagation test at the same rod displacement of 3 mm for the Fe-Al and Co-Al systems welded using three different welding speeds. The debonding crack propagates from the right to the left and its length is measured from the tip of the notch. The distance between the black marks on the side of the specimens is 5 mm (starting from the initial tip of the notch).

Fig. 7 shows the load-displacement curves measured during crack propagation tests. The reproducibility between the tested samples is excellent, justifying that only one curve is

provided per condition. The load reaches a maximum just before crack extension starts. For the Fe-Al system at a welding speed of 300 mm.min^{-1}, load-displacement curves show drops of the load (indicated with arrows in Fig. 7(a)). These drops are associated with the load relaxation brought about by the sudden propagation of the crack. The crack propagates more smoothly for higher welding speeds. The largest load values are found for the Al-Fe system at a welding speed of 700 mm.min^{-1} and for the Al-Co system at a welding speed of 500 mm.min^{-1}.

Fig. 8(a) shows the stress-strain curve of the steel sample processed by FMB. This curve is used in Eq. 5 to assess the energy dissipated during bending of the steel. The steel presents a martensitic microstructure resulting from the heat cycle carried out during the FMB processing. It differs from the typical microstructure of DP steel, i.e. a distribution of martensite islands in a ferritic matrix. Fig. 8(b) shows the evolution of the friction coefficient, μ, measured by tribometry as a function of the vertical load: μ increases as the load increases, but the travel speed has no significant influence. For obtaining the friction coefficients to be used in Eq. 7, the data of Fig. 8b were fitted by a linear law (dashed line) using least mean square statistics.

Figs. 9(a, b) show an example of the energy conservation calculation for a weld without plating welded at 700 mm.min^{-1} and for a weld with Co plating welded at 500 mm.min^{-1}, respectively. Each point on the curve corresponds to a frame of the video. For each frame, the curvature of the steel beam along its length, the crack length, the position of the rod and the contact angle between the rod and the steel beam are obtained by computer-aided analysis of the image. The blue circles correspond to the work made on the sample, E. They are calculated by integration of the load-displacement curves shown in Fig. 7. The red inversed triangles correspond to the energy, W_{steel}, dissipated by the deformation of the steel beam calculated via Eq. 5. The green triangles correspond to the friction dissipation, $W_{friction}$,

calculated via Eq. 7 using the friction coefficients, μ, given in Fig. 8(b). The black squares correspond to the energy dissipated specifically related to crack propagation and is calculated as $\Gamma = E - W_{steel} - W_{friction}$. The curves are fitted by a straight line covering the first linear regime after the crack starts to propagate using a least squares method. The fitted slope is then divided by the width of the steel beam, b, to obtain the critical energy release rate, Γ. Fig. 9(c) shows the calculated values of Γ for the Fe-Al and the Co-Al systems as a function of the mean of the IM layer thickness values measured in Fig. 5.

5.4. Crack observations and fractography

Fig. 10 illustrates the two types of crack propagation mode observed in the Fe-Al system. In the presence of the thick IM layer formed at a welding speed of 300 mm.min^{-1}, the crack fully propagates through the IM layer (Figs. 10(a, b)). SEM observation of the fracture surface shows evidence of a brittle mode of fracture by cleavage (Figs. 10(c, d)). In the presence of the thin IM layer formed at a welding speed of 700 mm.min^{-1}, SEM observation shows evidence of a combination of two modes of fracture (Figs. 10(e, f)): part of the fracture surface exhibits a ductile fracture mode with crack propagation through the Al plate whereas the other part exhibits a brittle fracture mode with crack propagation through the IM layer (Figs. 10(g, h)). The ductile fracture mode is characterised by dimples resulting from a sequence of ductile cavity formation, growth and coalescence. The brittle fracture mode is characterized by cleavage facets [28]. At both welding speeds, transverse cracks are observed in the IM layer ahead of the crack tip.

Fig. 11 illustrates crack propagation in the Al-Co system. At low welding speed (300 mm.min^{-1}), the crack propagates along the interface between the IM layer and the Co coating (Figs. 11(a, b)). Observations on the aluminium side of the fracture reveal a pattern of horizontal cracks in the IM layer originating from the bending of the specimen during the test (Fig. 11(c)). At higher magnification, SEM observation (Fig. 11(d)) reveals that the surface is

covered by faceted grains corresponding to the $CoAl_3$ intermetallic: EDX analysis confirms the presence of Co and Al. For a weld speed of 500 mm.min^{-1}, the crack fully propagates through the Al plate (Figs. 11(e, f)). Unlike the case of the Fe-Al system, no isolated region of brittle intermetallic fracture is observed on the surface (Fig. 11(g)). Observations at higher magnification reveal that the fracture mode is ductile, as attested by the presence of characteristic dimples (Fig. 11(h)). Similarly to the Fe-Al system, transversal cracks can be found in the IM layer ahead of the crack tip at both welding speeds.

For the Co-Al system at high welding speed (700 mm.min^{-1}), hot tears are observed in the aluminium plate below the interface, which lead to crack propagation along hot tear defects (Figs. 12(a, b)). Fig. 12(c) reveals that hot tear defects alternate with interface parts that fractured in a ductile way. A closer look at the hot tear surface in Fig. 12(d) reveals free solidification morphology.

6. Discussion

6.1. IM growth

Fe-Al intermetallic phases present a 'tongue-like' microstructure resulting from directional growth along the c-axis of the Fe_2Al_5 unit cell [29] (Figs. 3(a, b, c)). Co-Al intermetallic phases form a homogeneous layer. At a low welding speed, Co_2Al_9 crystals at the interface with the aluminium presents faceted grains (Fig. 3(d)).

The growth rate of the IM layer during reactive wetting is determined by two competitive phenomena: (i) the formation of the IM phase by reaction of Al with Fe; (ii) the dissolution of the IM phase into the liquid aluminium [30]. In the Fe-Al system, the growth of the IM phase mainly depends on the rate of formation of Fe_2Al_5, according to the mechanism well described by Tanaka *et al.* [8]. The mobility of Fe in the IM phase is negligible compared to the mobility of Al [31]. Al atoms diffuse through the IM layer from the aluminium side to the steel side where they react with the Fe atoms to form Fe_2Al_5, bringing an increase of the IM

layer thickness. Simultaneously, at the IM-Al interface, the dissolution phenomenon reduces the thickness of the IM layer [32]. The Co-Al systems shows lower IM layer thicknesses since the difference between growth and dissolution rates is smaller than in the case of the Fe-Al system, where growth clearly dominates over dissolution. At a speed of 300 mm.min^{-1}, the mean IM layer thicknesses in the Fe-Al and Co-Al systems are 8.0, and 2.5 µm, respectively, clearly demonstrating the beneficial role of Co on the reduction of IM layer thickness.

The kinetic constants of Eq. 3 for the Fe-Al system have been already assessed by other authors. The apparent activation energy calculated in the present work, Q = 268 kJ.mol^{-1} (Table 7) is larger than the values measured by other authors. Indeed, Yin *et al.* [7] measured Q = 207 kJ.mol^{-1} for the dipping of pure Fe into pure Al. Zhang *et al.* [33] calculated Q = 239 kJ.mol^{-1} in resistance spot welding of a galvanised steel to AA6008 alloy. Crucifix *et al.* [6] calculated Q = 200 kJ.mol^{-1} in FMB welding of ultra-low-carbon steel to AA2024 alloy. The presence of alloying elements in the base materials can modify the growth rate of the IM layer. This is the case for carbon in steel and for Si in aluminium, elements which are known to reduce the growth rate of the IM layer [7,15]. Another source of error in the evaluation of activation energy is the estimation of the temperatures at the interface from the finite element model. The unknown variables of the model are calibrated from measurements away from the molten pool [6,19] and no measurement can be made inside the molten pool and at the reacting interface.

6.2. Critical energy release rate during crack propagation

Both the nature of the interlayer and the welding speed have an influence on the cracking resistance of the weld. In the Fe-Al system, a transition occurs as the welding speed increases from an in-plane fracture path through the IM layer parallel to the interface (Fig. 10(a)) to an alternating crack path between the IM layer and the Al plate (Fig. 10(e)). The in-plane IM layer cracking occurs in the 8-µm thick IM layer obtained at a welding speed of

300 mm.min^{-1} and the critical energy release rate is evaluated of the order of 1 kJ.m^{-2}. Using the value of fracture toughness for Fe_2Al_5 (K_{IC} = 0.51 MPa.m$^{-0.5}$) measured by Kyokuta *et al.* [34], the Young's modulus of Fe_2Al_5 (E = 240 GPa) measured by Tsukahara *et al.* [35] and linear elastic fracture mechanics, the intrinsic critical energy release rate of the IM layer would be of the order of 1 J.m^{-2}, i.e. three orders of magnitude lower than the measured values. The crack path alternating in aluminium and IM layer is observed in the case of the 2-µm thick IM layer obtained at a welding speed of 700 mm.min^{-1}. The energy conservation method then yields a critical energy release rate of up to 8 kJ.m^{-2}. This value is close to toughness values measured for other aluminium alloys, i.e. over 10 kJ.m^{-2} [36].

The large differences between the measured toughness for a thick IM layer (approximately 1 kJ.m^{-2} for an 8-µm thick IM layer) and the intrinsic toughness of the IM phases (approximately 1 J.m^{-2}) can be explained by strain energy dissipation in the elasto-plastic substrates (steel and aluminium) around the crack tip during crack propagation as suggested by Kyokuta *et al.* [37]. They stated the critical stress needed to cause cracking of the IM layer between elasto-plastic substrates is a function of its thickness. A similar argument could be proposed in the case of an in-plane crack. Fig. 13 illustrates the cases where a centred crack propagates in a thick or a thin intermetallic layer embedded between two elasto-plastic plates. If the distance from the crack tip to the substrates is too large, the substrates are not significantly affected by the strain field around the tip of the crack (Fig. 13(a)). On the other hand, if the IM layer is thin, the distance between the substrates and the crack tip decreases and the substrates show a large plastic zone that dissipates more energy, hence increases the critical energy release rate (Fig. 13(b)).

Moreover, Figs. 10(a, e) and 11(a, e) show the presence of transverse cracks in the IM layer that are formed ahead of the crack tip as a result of the bending of the steel beam. The presence of such cracks tends to deviate the crack path from in-plane through the IM layer to

perpendicular towards the base materials where it propagates in a ductile manner. These two effects, the formation of a processed zone in the base materials and the deviation of the crack towards the aluminium plate, explain the larger toughness values measured for thin Fe-Al IM layers.

In the case of the Co-Al system, at a welding speed 500 $mm.min^{-1}$, the crack fully propagates within the Al plate, bringing slightly higher values of Γ than the ones measured for the Fe-Al system at 700 $mm.min^{-1}$ since no IM layer fracture is involved at all. In this case, the value of the critical energy release rate (up to 12 $kJ.m^{-2}$) is of the order of the values measured for some aluminium alloys [36].

6.3. Coating performance

As stated in the introduction, the IM layer thickness can be reduced by controlling the thermal cycles. For the case of the Fe-Al system, there is a window of welding speed that results in a thin continuous IM layer bringing high toughness. If the welding speed is too slow, the IM layer becomes too thick so that the toughness of the weld is largely decreased. If the welding speed is too fast, the heat input is not large enough to allow melting of the Al plate and the bonding reaction does not take place [19]. Since the growth rates of the Fe/Al aluminides are large, the window of useful welding speed is very narrow and the risk of facing any of the above-mentioned problems increases. In order to ease the control of the IM layer thickness, the choice of an interlayer should aim at providing an environment in which the growth rate of the IM layer is lower than that occurring in the Fe-Al system. In the present work, the use of Co greatly reduces this growth rate and IM layers.

The interlayer should also be chemically compatible with the base materials. More specifically, the interaction of the interlayer and the liquid aluminium should not induce solidification defects such as hot tears. In the present work, hot tears are due to the dissolution of the interlayer in the Al molten pool, which changes the composition of the liquid and

modifies the hot tearing susceptibility [37,38]. The dissolution of Co in the molten pool acts in such way that hot tears can be formed, which drastically affects the strength of the weld. Nevertheless, the formation of hot tears depends on welding parameters. Previous observations of hot tears in FMB [5,6,19] highlighted the fact that hot tears are more likely to form at high welding speeds. This means that the hot tearing risk is slightly increased by the dissolution of Co into the molten Al and the effects are only observed at high welding speeds, i.e. at 700 $mm.min^{-1}$.

Conclusions

The effect of Co interlayers has been investigated in Al-to-steel welds made by Friction Melt Bonding. The main results are the following:

1. With the use of Co plating, the nature of the intermetallic phases formed at the welded interface changes from a Fe_4Al_{13} - Fe_2Al_5 to Co_2Al_9 - $CoAl_3$.
2. The use of Co plating reduces the thickness of the IM layer by 70% when compared to a weld without interlayer.
3. The toughness of the interface was assessed by measuring the critical energy release rate via an adapted crack propagation test. In the case of a weld without interlayer the toughness is observed to increase as the IM layer thickness decreases. Critical energy release rates of the order of 1 $kJ.m^{-2}$ are measured for IM layer thicknesses over 8 µm (300 $mm.min^{-1}$). They increase up to 8 $kJ.m^{-2}$ when the thickness is reduced to 2 µm (700 $mm.min^{-1}$). When the IM layer is thick (~8 µm), the crack propagates in a brittle manner through the thickness of the IM layer. The increase in toughness for thin IM layer (~2 µm) is ascribed to a larger plastic dissipation around the crack tip in the base materials and to alternate crack propagation: in a ductile mode through the Al plate and in a brittle mode through the IM layer.

4. At intermediate welding speeds, 500 mm.min^{-1}, the Co/Al intermetallic layer formed with a Co plating is about 1.3 µm thick. In this case, the crack fully propagates through the Al plate in a ductile manner, which leads to the best critical energy release rate measured in this study, 11 kJ.m^{-2}. At lower welding speed (300 mm.min^{-1}), the crack propagates through the interface between the Co plating and the Co_2Al_9 IM layer, leading to critical energy release rates of the order of 1 kJ.m^{-2}, similar to the Fe-Al system at the same speed. At higher welding speeds (700 mm.min^{-1}), the critical energy release rate is drastically reduced by the presence of hot tears (1 to 7 kJ.m^{-2}).

Acknowledgements

The authors acknowledge the financial support of the Interuniversity Attraction Poles Program from the Belgian State through the Belgian Policy agency, contract IAP7/21 INTEMATE. N. Jimenez-Mena acknowledges the financial support of FRIA, Belgium. A. Simar acknowledges the financial support of ERC-StG, project ALUFIX, grant agreement n° 716678. H. Idrissi is mandated by the Belgian National Fund for Scientific Research (FSR-FNRS). The authors also acknowledge M. Coulombier for the help provided in the measurement of the friction coefficient, and T. Pardoen and F. Lani for the fruitful discussions.

References

[1] X. Cui, H. Zhang, S. Wang, L. Zhang, J. Ko, Design of lightweight multi-material automotive bodies using new material performance indices of thin-walled beams for the material selection with crashworthiness consideration, Mater. Des. 32 (2011) 815-821.
[2] U. Dilthey, L. Stein, Multimaterial car body design: challenge for welding and joining, Sci. Technol. Weld. Join. 11 (2006) 135–142.
[3] A. Van Alboom, B. Lemmens, B. Breitbach, F. De Grave, S. Cottenier, K. Verbeken, Multi-method identification and characterization of the intermetallic surface layers of hot-dip Al-coated steel: $FeAl_3$ or Fe_4Al_{13} and Fe_2Al_5 or Fe_2Al_{5+x}. Surf. Coat. Technol. 324 (2017) 419-428.
[4] T. Tanaka, T. Morishige, T. Hirata, Comprehensive analysis of joint strength for dissimilar friction stir welds of mild steel to aluminum alloys, Scr. Mater. 61 (2009) 756–759.
[5] C. Van der Rest, P.J. Jacques, A. Simar, On the joining of steel and aluminium by means of a new friction melt bonding process, Scr. Mater. 77 (2014) 25–28.

[6] S. Crucifix, C. Van Der Rest, N. Jimenez-Mena, P.J. Jacques, A. Simar, Modelling thermal cycles and intermetallic growth during friction melt bonding of ULC steel to aluminium alloy 2024-T3. Sci. Technol. Weld. Joining 20 (2015) 319-324.
[7] F.C. Yin, M.X. Zhao, Y.X. Liu, W. Han, Z. Li, Effect of Si on growth kinetics of intermetallic compounds during reaction between solid iron and molten aluminum, Trans. Nonferrous Met. Soc. China 23 (2013) 556–561.
[8] Y. Tanaka, M. Kajihara, Kinetics of isothermal reactive diffusion between solid Fe and liquid Al, J. Mater. Sci. 45 (2010) 5676–5684.
[9] V. Jindal, V.C. Srivastava, A. Das, R.N. Ghosh, Reactive diffusion in the roll bonded iron-aluminum system, Mater. Lett. 60 (2006) 1758–1761.
[10] P. Peyre, G. Sierra, F. Deschaux-Beaume, D. Stuart, G. Fras, Generation of aluminium-steel joints with laser-induced reactive wetting, Mater. Sci. Eng. A. 444 (2007) 327–338.
[11] M. Winnicki, A. Małachowska, M. Korzeniowski, M. Jasiorski, A. Baszczuk, Aluminium to steel resistance spot welding with cold sprayed interlayer, Surf. Eng. 34 (2017) 235-242.
[12] S. Chen, J. Huang, K. Ma, H. Zhang, X. Zhao, Influence of a Ni-foil interlayer on Fe/Al dissimilar joint by laser penetration welding, Mater. Lett. 79 (2012) 296–299.
[13] S. Meco, L. Cozzolino, S. Ganguly, S. Williams, N. McPherson, Laser welding of steel to aluminium: Thermal modelling and joint strength analysis. J. Mater. Process. Technol. 247 (2017) 121-133.
[14] K. Ikeuchi, M. Takahashi, H. Watanabe, M. Aritoshi, Effects of carbon content on intermetallic compound layer and joint strength in friction welding of Al alloy to steel, Weld. World. 53 (2009) 135–139.
[15] S.H. Hwang, J.H. Song, Y.S. Kim, Effects of carbon content of carbon steel on its dissolution into a molten aluminum alloy, Mater. Sci. Eng. A. 390 (2005) 437–443.
[16] M.G. Reddy, S.A. Rao, T. Mohandas, Role of electroplated interlayer in continuous drive friction welding of AA6061 to AISI 304 dissimilar metals, Sci. Technol. Weld. Join. 13 (2008) 619–628.
[17] P.K. Sahu, S. Pal, S.K. Pal, Al/Cu Dissimilar Friction Stir Welding with Ni , Ti , and Zn foil as the interlayer for flow control enhancing mechanical and metallurgical properties, Metall. Mater. Trans. A. 48 (2017) 3300–3317.
[18] C. Van der Rest, A. Simar, P.J. Jacques, Method for welding at least two layers World patent WO2013164294. 2013 Nov 7.
[19] N. Jimenez-Mena, P.J. Jacques, J.M. Drezet, A. Simar, On the Prediction of Hot Tearing in Al-to-Steel Welding by Friction Melt Bonding, Metall. Mater. Trans. A 49 (2018) 2692-2704.
[20] Dassault Systems, Abaqus 6.14 Documentation, Providence, 2013.
[21] A. Bejan, Heat transfer, first ed., John Wiley & Sons, Hoboken, 1993.
[22] W. Rohsenow, J. Hartnett, Y. Cho, Handbook of Heat Transfer, third ed., McGraw-Hill, New York, 1998.
[23] S. Rimovskis, A. Sabaliauskas, Analysis of rectangular and circular cross-section power hardening elements under pure bending, Int. J. Mater. Eng. 2 (2012) 84–89.
[24] R, Cardona, M. Geradin, A beam finite element non-linear theory with finite rotations, Int. J. Numer. Meth. Eng. 26 (1988) 2403-2438
[25] A. Ramalho, J.C.Miranda, The relationship between wear and dissipated energy in sliding systems, Wear 260 (2006) 361-367
[26] NPCS Board of Consultants & Engineers, Electroplating, Anodizing & Metal Treatment Hand Book, Asia Pacific Business Press Inc, New Delhi, 2003.

[27] M. Rappaz, J. Drezet, M. Gremaud, A New Hot-Tearing Criterion, Metall. Mater. Trans. A Phys. Metall. Mater. Sci. 30 (1999) 449–455.
[28] A. Pineau, A.A. Benzerga, T. Pardoen, Failure of metals I: Brittle and ductile fracture, Acta Mater. 107 (2016) 424–483.
[29] N. Takata, M. Nishimoto, S. Kobayashi, M. Takeyama, Crystallography of Fe_2Al_5 phase at the interface between solid Fe and liquid Al, Intermetallics 67 (2015) 1-11.
[30] V.N. Yeremenko, Y. V. Natanzon, V.I. Dybkov, The effect of dissolution on the growth of the Fe_2Al_5 interlayer in the solid iron -liquid aluminium system, J. Mater. Sci. 16 (1981) 1748–1756.
[31] A. Bouayad, C. Gerometta, A. Belkebir, A. Ambari, Kinetic interactions between solid iron and molten aluminium, Mater. Sci. Eng. A. 363 (2003) 53–61.
[32] S. Chen, D. Yang, M. Zhang, J. Huang, X. Zhao, Interaction Between the Growth and Dissolution of Intermetallic Compounds in the Interfacial Reaction Between Solid Iron and Liquid Aluminum, Metall. Mater. Trans. A 47 (2016) 5088–5100.
[33] W. Zhang, D. Sun, L. Han, W. Gao, X. Qiu, Characterization of intermetallic compounds in dissimilar material resistance spot welded joint of high strength steel and aluminum alloy, ISIJ Int. 51 (2011) 1870–1877.
[34] N. Kyokuta, M. Koba, T. Araki, S. Nambu, J. Inoue, T. Koseki, Fracture toughness evaluation of thin Fe-Al intermetallic compound layer at reactive interface between dissimilar metals, Journal Japan Inst. Met. 76 (2012) 272–277.
[35] T. Tsukahara, N. Takata, S. Kobayash, M. Takeyama, Mechanical properties of Fe_2Al_5 and $FeAl_3$ intermetallic phases at ambient temperature. Tetsu to Hagane 102 (2016) 29-35.
[36] R.J. Bucci, Selecting aluminium alloys to resist failure by fracture mechanisms. Eng. Frac. Mech., 12 (1979) 407-441.
[37] J.M. Drezet, D. Allehaux, Application of the rappaz-drezet-gremaud hot tearing criterion to welding of aluminium alloys, in T. Boellinghaus, H. Herold (Eds.), Hot cracking phenomena in welds II, Springer, Berlin, 2008, pp. 27-45.
[38] Y. Tian, J.D. Robson, S. Riekehr, N. Kashaev, L. Wang, T. Lowe, A. Karanika, process optimization of dual-laser beam welding of advanced Al-Li Alloys Through Hot Cracking Susceptibility Modeling, Metall. Mater. Trans. A Phys. Metall. Mater. Sci. 47 (2016) 3533–3544.

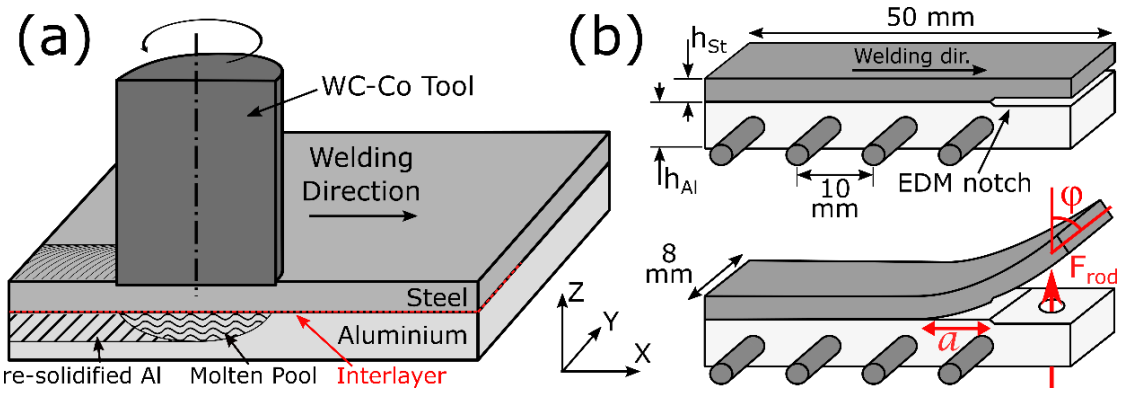

Fig 1: (a) Schematic representation of (a) the FMB process; (b) of the crack propagation tests. F_{rod} represents the load provided by the pushing rod and a represents the crack length measured from the tip of the notch.

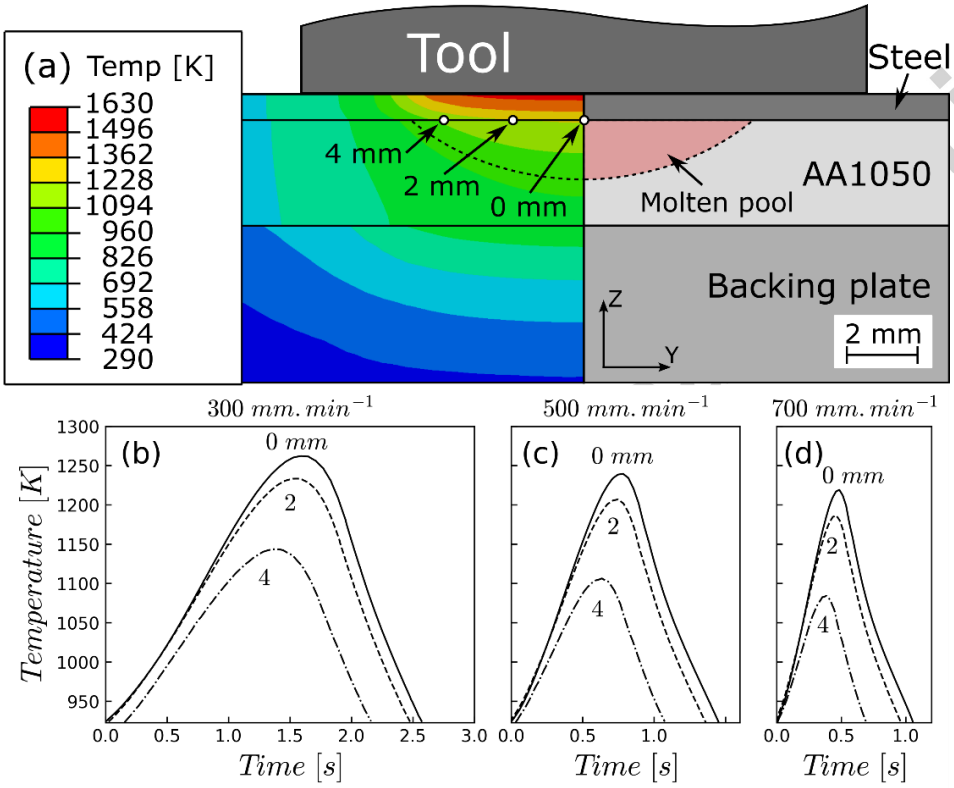

Fig 2: (a) Transversal cross cut view of a simulation of the thermal fields using Abaqus [20] for a weld performed at 700 mm.min^{-1}. (b, c and d) Temperature profiles as a function of time at the steel-aluminium interface from the simulations at 3 different distances from the weld centreline (0 mm, 2 mm and 4 mm) at welding speeds of (b) 300, (c) 500 and (d) 700 mm.min^{-1}. The coordinate system (Y, Z) refers to Fig. 1.

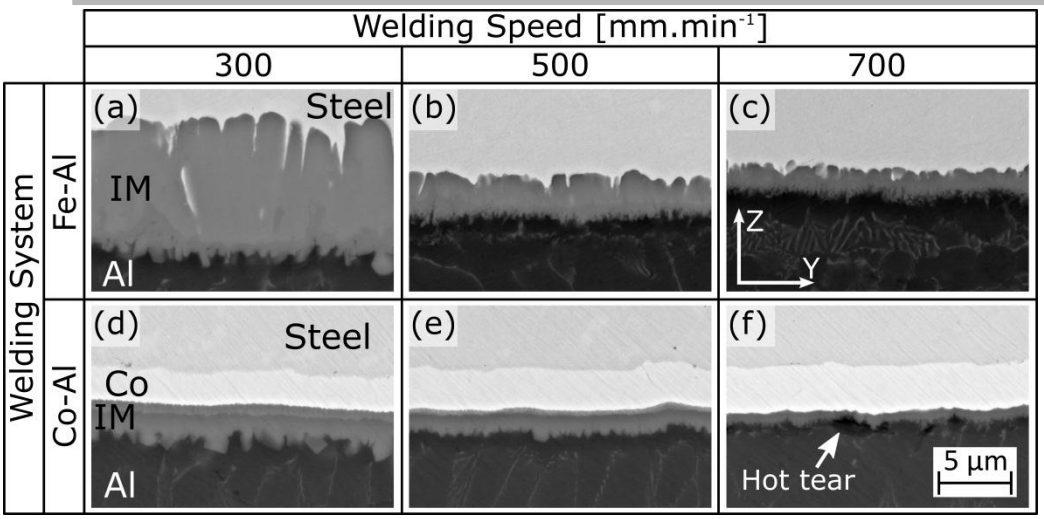

Fig 3: Backscatter SEM micrographs of the intermetallic phases formed at the interface for the Fe-Al and Co-Al welding systems with welding speeds of 300, 500 and 700 mm.min^{-1}.

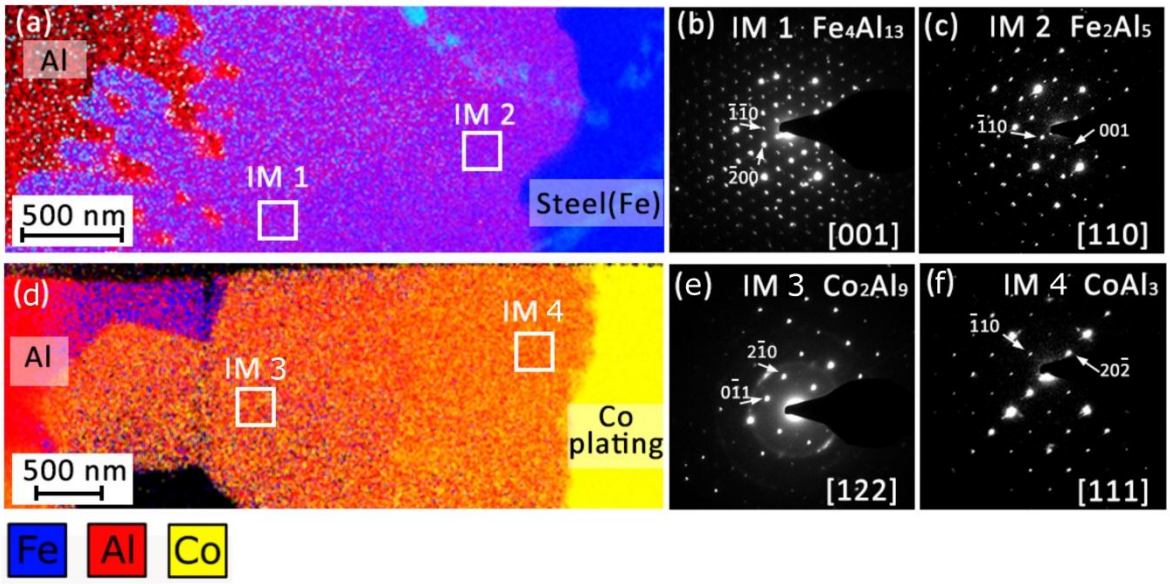

Fig 4: (a and d) EDX elemental maps acquired on FIB samples of the Fe-Al and Co-Al systems, respectively. (b, c, e and f) are SAED patterns obtained on IM1, IM2, IM3 and IM4, respectively, with indicated zone axis corresponding to the identified phase.

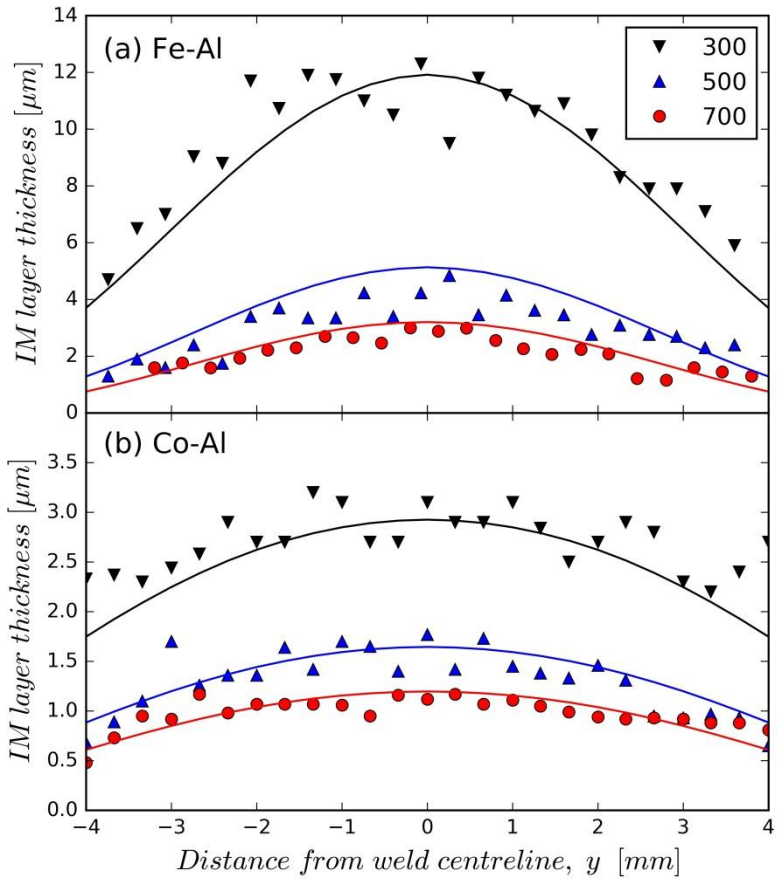

Fig 5: Thickness of the IM layer in the (Y, Z) plane (defined in Fig. 1). The points represent the measured thickness from the SEM images. The continuous lines are drawn using Eqs. 2 and 3 with the fitted parameters given in Table 7 and the temperature field from the FE simulations. Results are provided for the welding systems, (a) Fe-Al, and (b) Co-Al, at three welding speeds (300, 500 and 700 mm.min^{-1}).

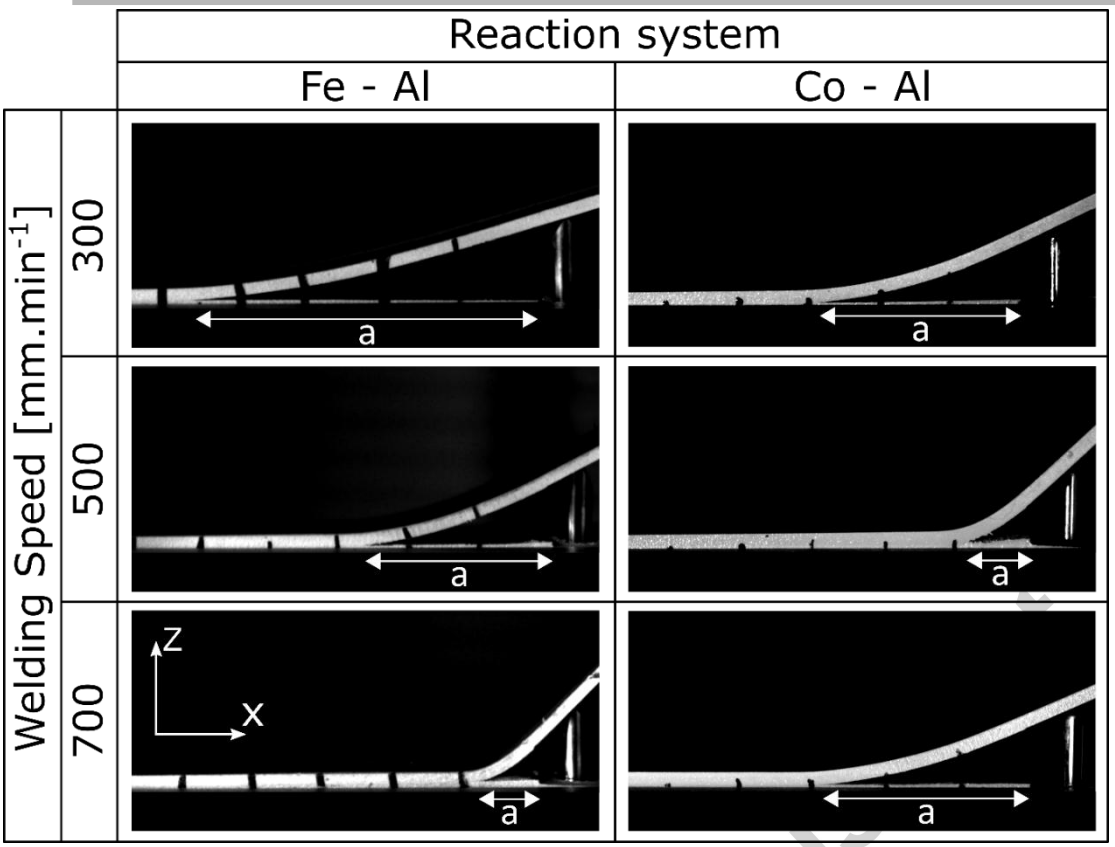

Fig 6: Frames from the video recording of the crack propagation test at a constant rod displacement of 3 mm for the Fe-Al and Co-Al systems at three different welding speeds (300, 500 and 700 mm.min^{-1}). The horizontal black marks on the specimens are spaced of 5 mm starting from the tip of the notch.

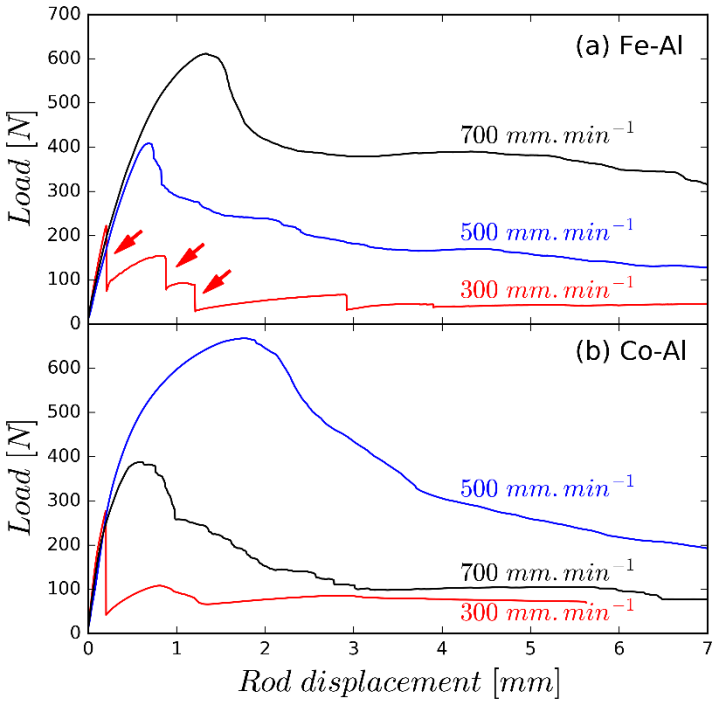

Fig 7: Load-displacement curves of the pushing rod measured during the crack propagation tests for the (a) Fe-Al and (b) Co-Al systems. The red arrows denote a sudden brittle propagation of the crack at 300 mm.min^{-1} in the Fe-Al system.

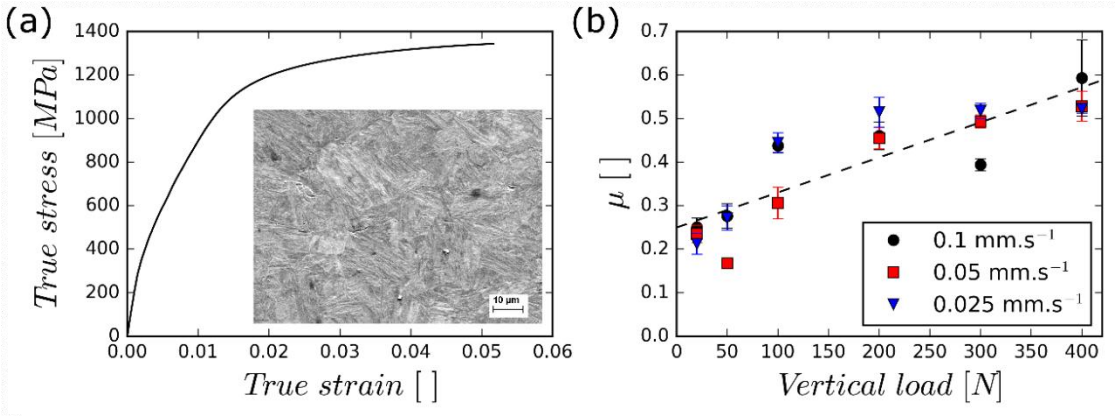

Fig 8: Data used for the calculation of Γ. (a) Stress-strain curve of the steel. The insert shows the martensitic microstructure after processing and (b) evolution of the friction coefficient, µ, as a function of the vertical load for various travel speeds.

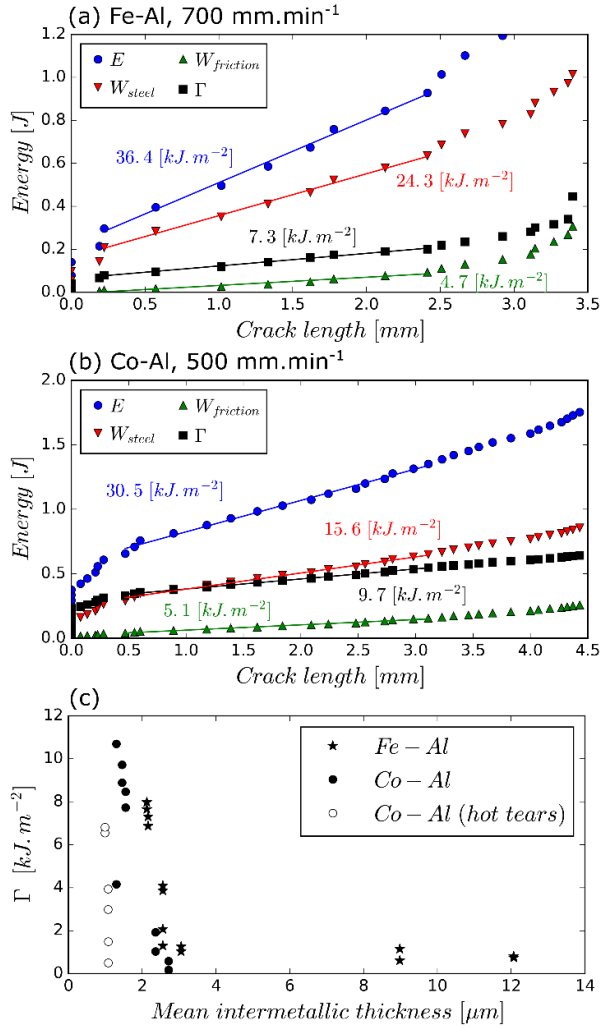

Fig 9: Calculation of the critical energy release rate, Γ, on (a) a Fe-Al specimen welded at 700 mm.min^{-1} and (b) a Co-Al specimen welded at 500 mm.min^{-1}. Each point of the curve corresponds to a frame of the video recording. The continuous lines correspond to the linear fit. (c) Calculated critical energy release rates, Γ, for the Fe-Al and the Co-Al systems as a function of the mean IM layer thickness. The empty marks denote the presence of hot tears in the specimen.

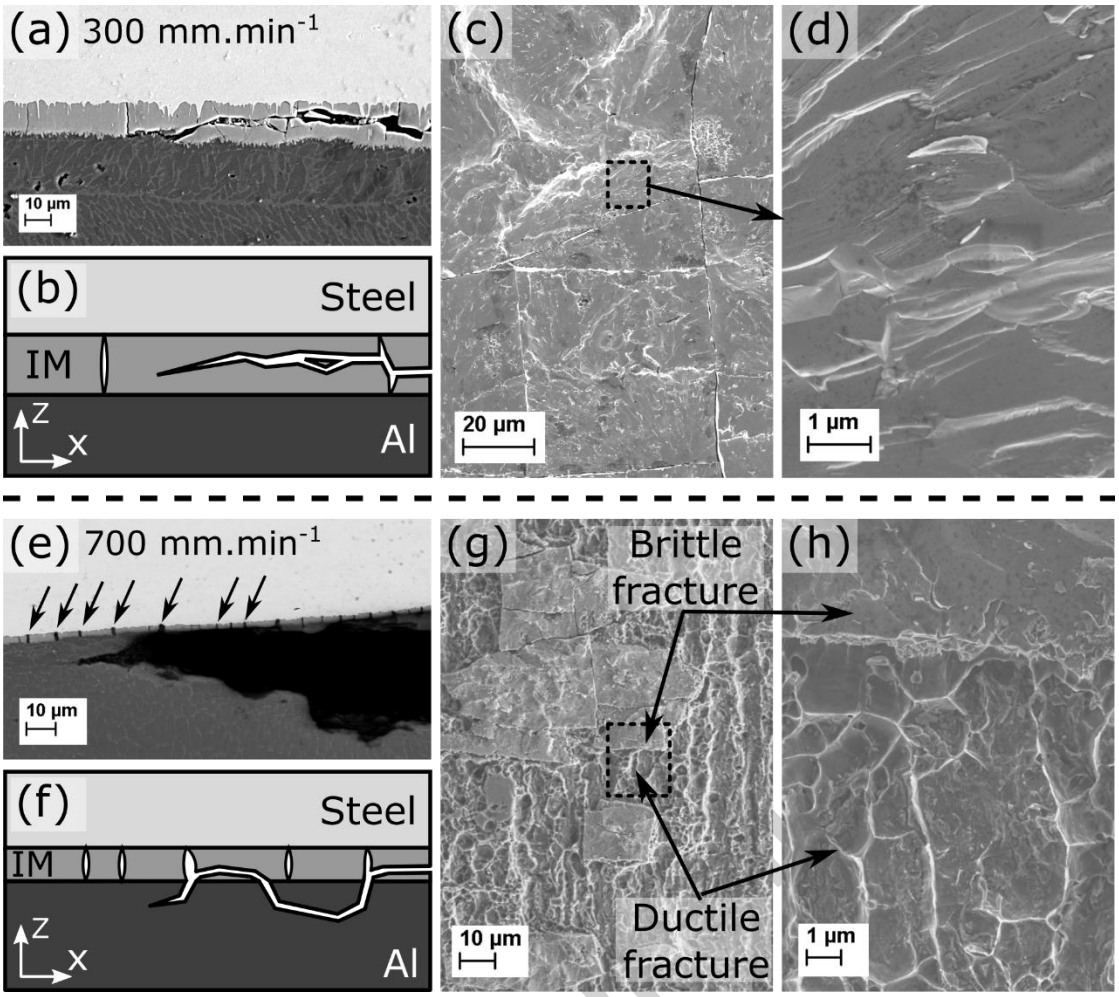

Fig 10: Crack and surface observations for the Fe-Al system corresponding to a weld performed at (a, b, c and d) 300 mm.min^{-1} and (e, f, g and h) 700 mm.min^{-1}. (a and b) Longitudinal cross section and schematic representation of the crack propagation through the IM layer, respectively. (c and d) Surface observations of the fracture revealing a brittle fracture at low and high magnification respectively. (e and f) Longitudinal cross section and schematic representation of the alternating crack propagation through the Al plate and the IM layer, respectively. (g and h) Surface observations of the fracture surface revealing a ductile fracture at low and high magnification respectively.

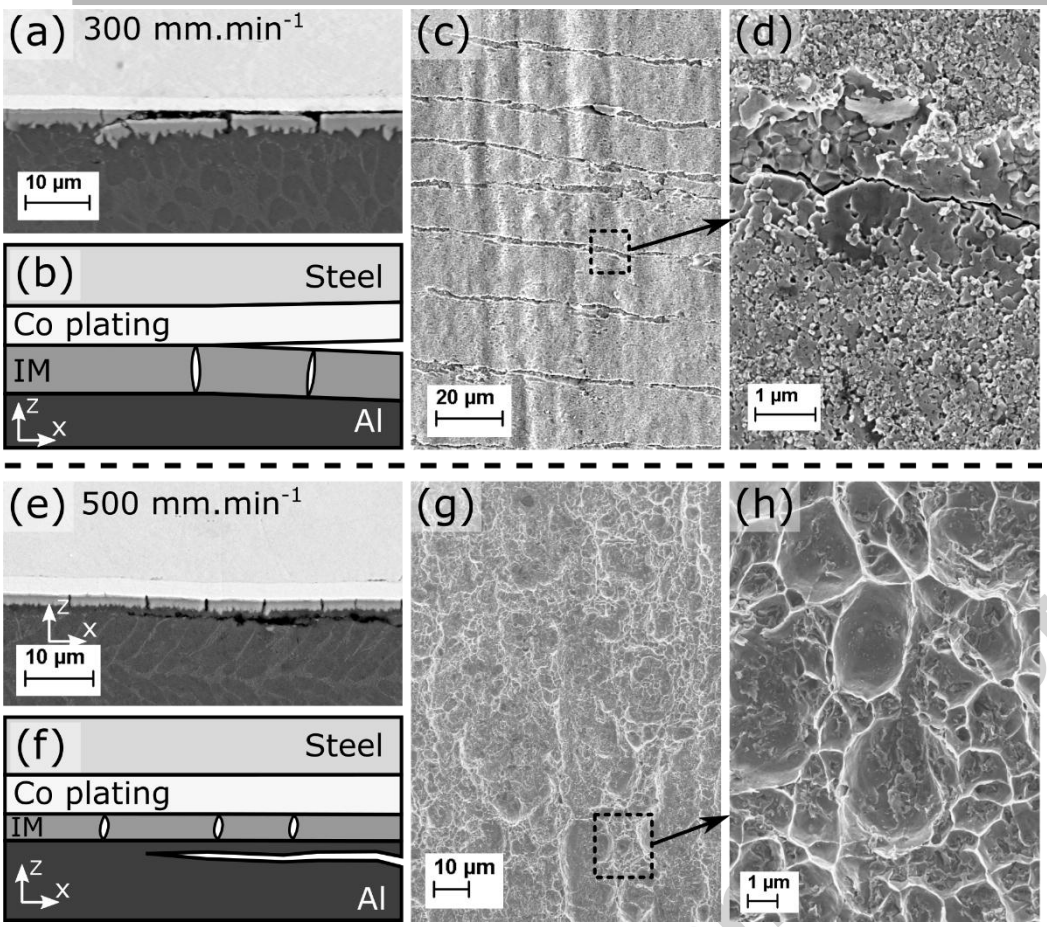

Fig 11: Crack and surface observations for the Co-Al system corresponding to a weld performed at (a, b, c and d) 300 mm.min^{-1} and (e, f, g and h) 500 mm.min^{-1}. (a and b) Longitudinal cross section and schematic representation of the crack propagation through the IM-plating, respectively. (c and d) Surface observations of the fracture revealing the faceted $Al_{13}Co_4$ grains on the Al side of the fracture. (e and f) Longitudinal cross section and schematic representation of the crack propagation through the Al, respectively. (g and h) Surface observations of the fracture surface revealing a ductile fracture characterised by dimples at low and high magnification respectively.

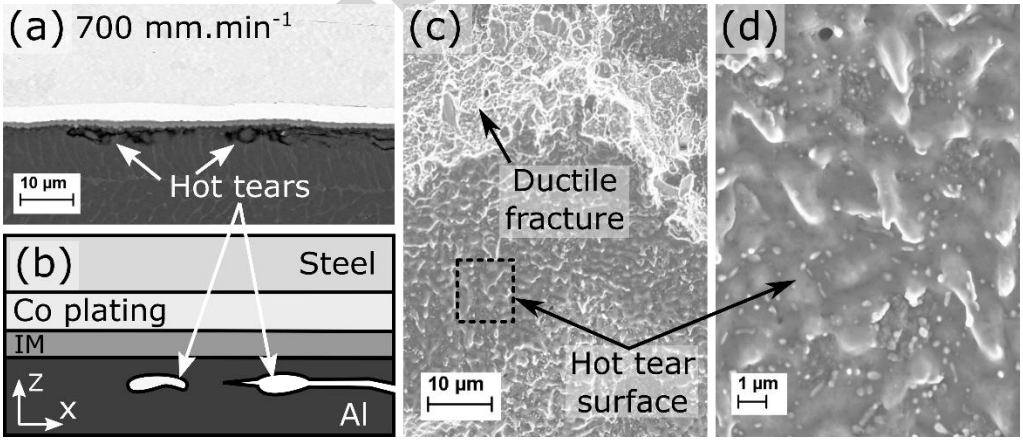

Fig 12: Crack and surface observations for a weld with a Co interlayer at 700 mm.min^{-1}. (a and b) Longitudinal cross section and schematic representation, respectively, of the crack propagation through the Al and the hot tear defects. (c) Surface observation of the fracture surface revealing a combination of hot tears and ductile fracture surfaces. (d) Observation at high magnification of the surface of a hot tear showing a solidification structure.

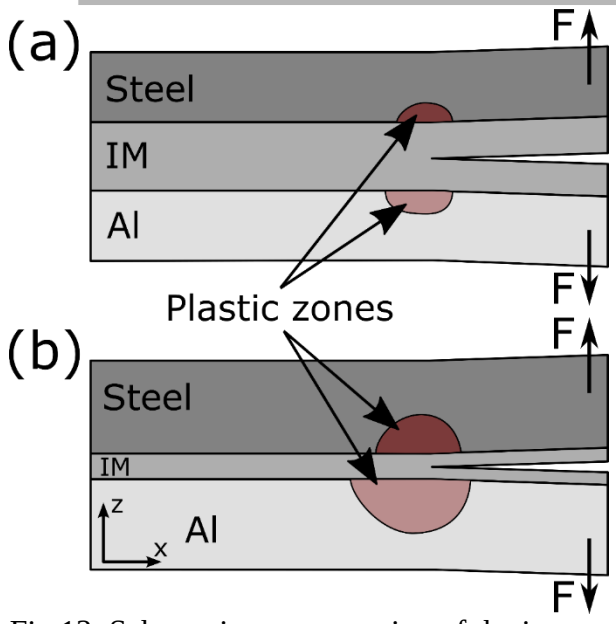

Fig 13: Schematic representation of the increase of plastic zone size in the base materials for welds with a (a) thick and (b) thin IM layer, respectively.

Table 1: Nomenclature

Symbol	Description	Units
a	Crack length	m
b	Width of the specimen	m
E	Energy exerted by the pushing rod	J
$F_{rod}, F_{\perp}$	Load in the pushing rod and perpendicular to the steel beam, respectively	N
h_{st}, h_{Al}	Thickness of the steel and aluminium, respectively	m
$k(\theta)$	Kinetic constant for IM layer growth	$m^2.s^{-1}$
k_o	Pre-exponential factor	$m^2.s^{-1}$
l	Relative displacement of the rod and the steel beam	m
Q	Activation energy	$J.mol^{-1}$
R	Gas constant	$J.mol^{-1}.K^{-1}$
t	Time	s
T_z	Torque on the tool	N.m
$W_{st}, W_{Al}, W_{friction}$	Dissipated energy on the steel, aluminium and by friction, respectively	$J.m^{-1}$
X	IM thickness	m
Γ	Critical energy release rate	$J.m^{-2}$
ε	Strain in the steel beam	-
η	Efficiency of the heat generation on the tool	-
θ	Temperature	K
μ	Friction coefficient	-
ρ	Radius of curvature	m
σ	Stress in the steel beam	Pa
φ	Angle between the rod and the steel beam	Degrees
ω	Rotational speed of the tool	$Rad.s^{-1}$

Table 2: Composition in % wt. of the base materials measured by induced coupled plasma (ICP)

	Al	Fe	Si	Ti	Mn	Ga	V	C	Cr
AA1050	Rest	0.38	0.06	0.01	0.01	0.01	0.01	-	-
DP600	0.02	Rest	0.21	0.02	1.96	-	-	0.16	0.19

Table 3: Process parameters and power input during welding. The power input has been inferred from the torque measurements on the tool using Eq. 1.

Welding speed [mm.min^{-1}]	Tool plunge [mm]	Power input [kW]
300	-0.11	3.6 ± 0.1
500	-0.16	4.0 ± 0.2
700	-0.19	4.4 ± 0.1

Table 4: Composition of the Co electroplating bath [26].

Reactive	$CoSO_4 \cdot 7H_2O$	NaCl	H_3BO_3
Concentration [g.l^{-1}]	400	17	45

Table 5: Parameters for electroplating [26]

Temperature [ºC]	Current density [A.cm^{-2}]	Time [s]
25	4.2 x 10^{-2}	370

Table 6: EDX composition measurement of the IM layers shown in Fig. 4. The measurements were obtained in the zones indicated by white squares in Fig. 4.

Intermetallic	Al (% at.)	Fe (% at.)	Co (% at.)
IM1 (Fe_4Al_{13})	70.3 ± 2	27.2 ± 2	-
IM2 (Fe_2Al_5)	67.1 ± 2	32.1 ± 2	
IM3 (Co_2Al_9)	75.8 ± 3	5.5 ± 5	18.7 ± 3
IM4 ($CoAl_3$)	71.8 ± 3	3.4 ± 2	24.8 ± 3

Table 7: Fitted values for k_o and Q in Eq. 3.

System	k_o (m^2.s^{-1})	Q (J.mol^{-1})
Fe-Al	9.5	2.68 x 10^5
Co-Al	2.89 x 10^{-7}	1.17 x 10^5